Microstructural Characterization of Self-Propagating High-Temperature Synthesis/ Dynamically Compacted and Hot-Pressed Titanium Carbides

KENNETH S. VECCHIO, JERRY C. LaSALVIA, MARC A. MEYERS, and GEORGE T. GRAY III

Titanium-Carbide produced by combustion synthesis followed by rapid densification in a high-speed forging machine was characterized by optical microscopy, scanning electron microscopy, and transmission electron microscopy (TEM). The density of the combustion synthesized/dynamically compacted TiC reached values greater than 96 pct of theoretical density, based on $TiC_{0.9}$, while commercially produced hot-pressed TiC typically exceeded 99 pct of theoretical density. The higher density of the hot-pressed TiC was found to be attributable to a large volume fraction of heavy element containing inclusions. The microstructure of both TiCs consists of equiaxed TiC grains with some porosity located both at grain boundaries and within the grain interiors. In both cases, self-propagating high-temperature synthesis (SHS)/dynamically compacted (DC) and hot-pressed, the TiC is ordered cubic (NaCl-structure, B_1; Space Group Fm3m) with a lattice parameter of ≈0.4310 nm, indicative of a slightly carbon deficient structure; stoichiometric TiC has a lattice parameter of 0.4320 nm. For the most part, the grains were free of dislocations, although some dislocation dipoles were found associated with the voids within the grain interiors. In one SHS/DC specimen, a new, complex Ti-Al-O(C) phase was observed. The structure could not be matched with any previously published phases but is believed to be hexagonal, with a c-axis/a-axis ratio of ≈6.6, similar to the $AlCTi_2$ phase which has a point group 6 mmm. In all other SHS/DC TiC samples, the grains and grain boundaries were devoid of any second-phase particles. The hot-pressed TiC exhibited a greater degree of porosity than the SHS/densified specimens and a large concentration of second-phase particles at grain boundaries and within grains. The structure and composition of these second-phase particles were determined by convergent beam electron diffraction (CBED) and X-ray microanalysis.

I. INTRODUCTION

COMBUSTION synthesis, reaction synthesis, or self-propagating high-temperature synthesis (SHS) are methods of producing ceramics and intermetallics that are receiving a great deal of attention. An early example of this synthesis method is the thermite reaction used to join train rails. In the thermite reaction, an Fe_2O_3 + Al mixture reacts exothermally, producing Al_2O_3 and Fe as a weld metal. Extensive investigations in the Soviet Union by Merzhanov and co-workers[1,2,3] have yielded over 300 compounds produced by this method, and a number of industrial processes have resulted. This collection of work inspired a considerable amount of interest within the United States, and Frankhouser *et al.*'s monograph[4] provides a thorough analysis of the early Soviet work. There are currently a number of on-going efforts in the United States, Japan, and Western Europe; a comprehensive review of this work has been provided by Munir and Anselmi-Tomburini.[5]

As part of a program intended to synthesize ceramics by combustion synthesis followed by consolidation, titanium carbide disks were produced by a novel method of combining SHS and dynamic forging, which is described in greater detail by LaSalvia *et al.*[6] and Meyer *et al.*[7] The use of dynamic consolidation in a high-speed forging machine after the conclusion of the combustion reaction (5 to 15 seconds) enabled the collapse of the porosity of the as-synthesized product while it was still hot and ductile. Earlier work by Niiler *et al.*[8] had shown that full densification could be accomplished by SHS followed by explosive compaction. The densification process is required because combustion synthesis produces a product with approximately 50 pct porosity. Figure 1 shows a polished section of titanium carbide produced by SHS without subsequent compaction, demonstrating the porous nature of the SHS reaction product; the dark areas in the micrograph represent the voids. There are three sources of porosity: (a) the initial porosity of the powder mixture prior to the reaction; (b) the shrinkage associated with the reaction (*i.e.*, products that have a higher specific volume than the starting reactants); and (c) the formation of gases in conjunction with the reaction, and their subsequent expansion, entrapment, or escape. Indeed, one often observes a considerable increase in the dimensions of the SHS product compared with the reactants.

KENNETH S. VECCHIO, Assistant Professor, JERRY C. LaSALVIA, Graduate Student, and MARC A. MEYERS, Professor, are with the Department of AMES, University of California, San Diego, LaJolla, CA 92093. GEORGE T. GRAY III, Staff Member, is with Los Alamos National Laboratory, Los Alamos, NM 87545.

This paper is based on a presentation made in the symposium "Reaction Synthesis of Materials" presented during the TMS Annual Meeting, New Orleans, LA, February 17–21, 1991, under the auspices of the TMS Powder Metallurgy Committee.

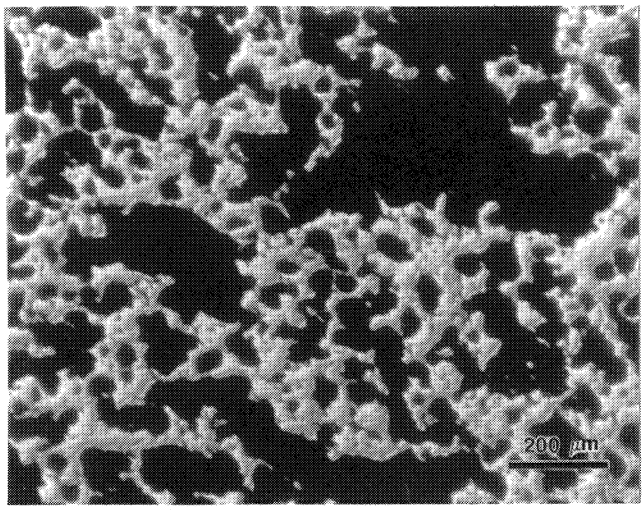

Fig. 1 — Optical micrograph of cross section through titanium carbide produced by SHS without consolidation. Dark regions represent voids present in the reacted product.

The high density of pores created during the SHS reaction is the motivation for attempting consolidation. However, in order to consolidate the SHS product, compaction must be conducted with the product at a temperature above the ductile-to-brittle transition. If the compaction is conducted immediately after the reaction, while the product is still at high temperature, consolidation can be accomplished without additional heating, making the process more energy efficient. As such, dynamic forging of the SHS product immediately after reaction offers the ability to achieve significant densification before cooling can take place, and without the need for additional heating.

The purposes of this study were to characterize the microstructure of TiC produced by the combination of SHS followed by dynamic compaction (hereafter denoted as "SHS/DC-TiC") and to compare this microstructure with the microstructure of commercially hot-pressed TiC (hereafter denoted as "HP-TiC"). In addition, the relationship between the microstructure of both forms of TiC (SHS/DC and HP) and physical properties, in particular, density, needs to be established in order to assess the success of this novel processing technique for the production of high-quality TiC.

II. EXPERIMENTAL PROCEDURE

A detailed description of the experimental procedure for producing SHS/DC disks of TiC has been given by Meyer *et al.*[7] The basic parameters for the selection, preparation, and pressing of powders, initiation of the reaction, and containment were developed by Niiler *et al.*[8] Titanium powder, with a 325 mesh (<44 μm) size, and carbon powder (≈2 μm size) were mixed, dry, in a ball mill for 8 to 10 hours. The composition selected was $TiC_{0.9}$, because Niiler *et al.*[8] showed that this was easier to compact than the stoichiometric TiC composition. The $TiC_{0.9}$ remains in the single-phase (gamma) field for cubic TiC within the Ti-C binary system.

After mixing, disk-shaped specimens (100-cm diameter and 12-cm height) were obtained by pressing the powders uniaxially to a pressure of approximately 50 MPa, yielding a green compact with a density of 60 pct; the combustion wave velocity is dependent on porosity, and the above density level was found experimentally to provide the best combustion conditions. The green compacts were then placed in a specially designed die of a high-speed forging machine. The combustion reaction was initiated at the top of the green compact by placing a small quantity of the loose Ti and C powders on the surface and igniting the reactant powders with an electric match. Upon completion of the reaction, the forging machine (described by Meyer *et al.*[7] and Hoke *et al.*[9]) was activated and the forging hammer descended upon the reacted product, forging it at velocities varying between 10 and 15 m/s. After densification, the compacts were placed in a furnace at 1100 °C under controlled argon atmosphere for slow cooling over a period of 12 hours.

The HP-TiC was produced by CERCOM in Vista, CA by conventional hot-pressing techniques. The titanium and carbon were standard production powders obtained from Hermann Starck, Inc., New York, NY, and were hot-pressed at 1800 °C to 1900 °C and 21 MPa for 1 hour.

The density of the TiC materials was determined using Archimedes' principle, and a theoretical density was calculated based on the composition $TiC_{0.9}$. The percent of theoretical density is then taken simply as the ratio of the experimental density to the theoretical density.

Specimens of both SHS/DC- and HP-TiC were prepared for optical microscope and scanning electron microscope (SEM) examination using diamond-based grinding and polishing techniques. Specimens for optical inspection were chemically etched in a solution of (by volume) 50 pct nitric acid, 25 pct hydrofluoric acid (40 pct), and 25 pct acetic acid for times up to 1 minute. Specimens for SEM evaluation were examined unetched using secondary electron imaging in order to better image the porosity present while still obtaining grain-to-grain contrast *via* electron channeling (normally a backscattered electron technique).

Specimens for transmission electron microscopy (TEM) were prepared by ultrasonically cutting 3-mm-diameter cylinders from bulk samples, followed by slicing on a slow-speed diamond saw into 0.5 mm-thick disks. These disks were then ground to 200 μm, dimpled to 50 μm, and finally, ion-milled to electron transparency at 6 kV and 1 mA gun current in a Gatan dual-stage ion-mill with the specimen cooled to approximately liquid nitrogen temperature.

Transmission electron microscopy analysis was conducted in a PHILIPS* CM30 electron microscope and X-ray microanalysis performed with a Link Analytical AN1085 system using an LZ5 ultrathin window detector. Conventional TEM imaging and diffraction, as well as X-ray microanalysis, were conducted at 300 kV, while all convergent beam electron diffraction (CBED) was conducted at 100 kV accelerating potential. Thin foil specimens of pure Cu were used to obtain CBED patterns from a material of known lattice constant in order

*PHILIPS is a trademark of Philips Electronic Instruments Corp., Mahwah, NJ.

to standardize the microscope accelerating voltage for subsequent CBED lattice parameter measurements of the TiC specimens. All CBED patterns for lattice parameter measurements were recorded along the [114] orientation, and higher order Laue zone (HOLZ) line simulations were performed using the public domain program DFTools written by John Sutliff. The accuracy of the CBED HOLZ line technique for lattice parameter measurements has been shown to be 0.0002 nm experimentally, and guidelines for the use of this technique have been outlined recently by Vecchio.[10]

III. RESULTS AND DISCUSSION

A. *Optical and SEM Observations*

Figure 2 shows optical micrographs of polished and etched sections of titanium carbide produced by SHS/DC and hot-pressing, (a) and (b), respectively. The SHS/DC material shows an equiaxed grain structure, indicating that this grain structure was produced after the compaction process. If the grains existed prior to compaction, it would be expected that the grain structure would

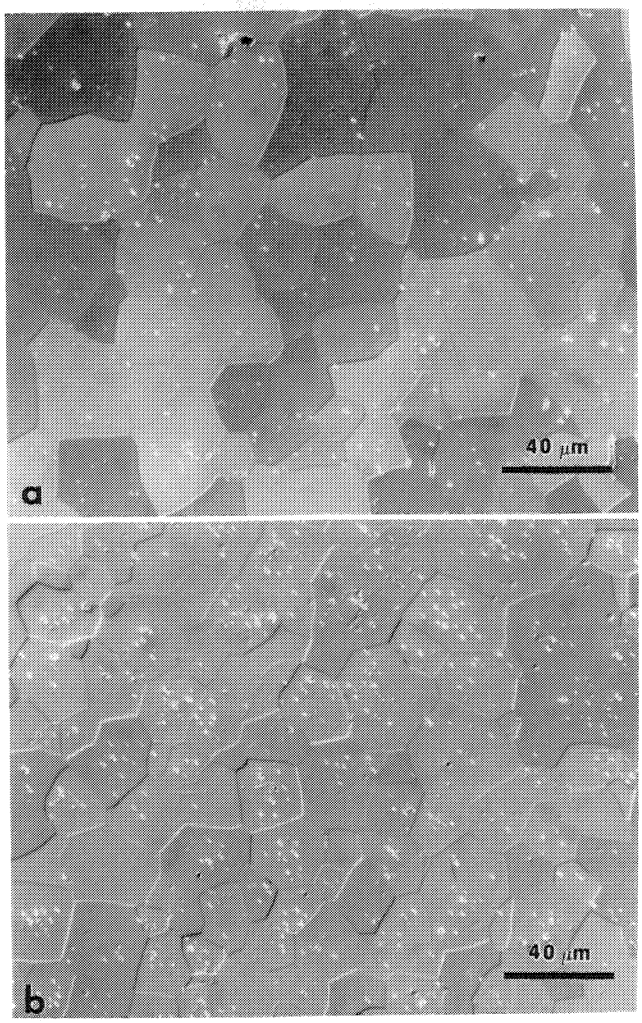

Fig. 2—Optical micrograph of (*a*) SHS/DC-TiC and (*b*) HP-TiC showing equiaxed grain structure for both materials.

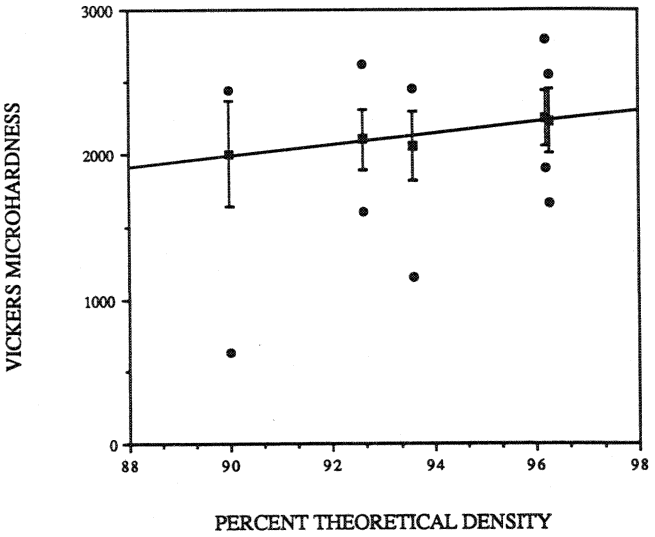

Fig. 3—Plot of Vickers hardness data as function of density for the SHS/DC-TiC material. The data shown with error bars indicate the mean and standard deviation of the hardness, while the data above the error bars indicate maximum hardness and those below the error bars represent minimum hardness.

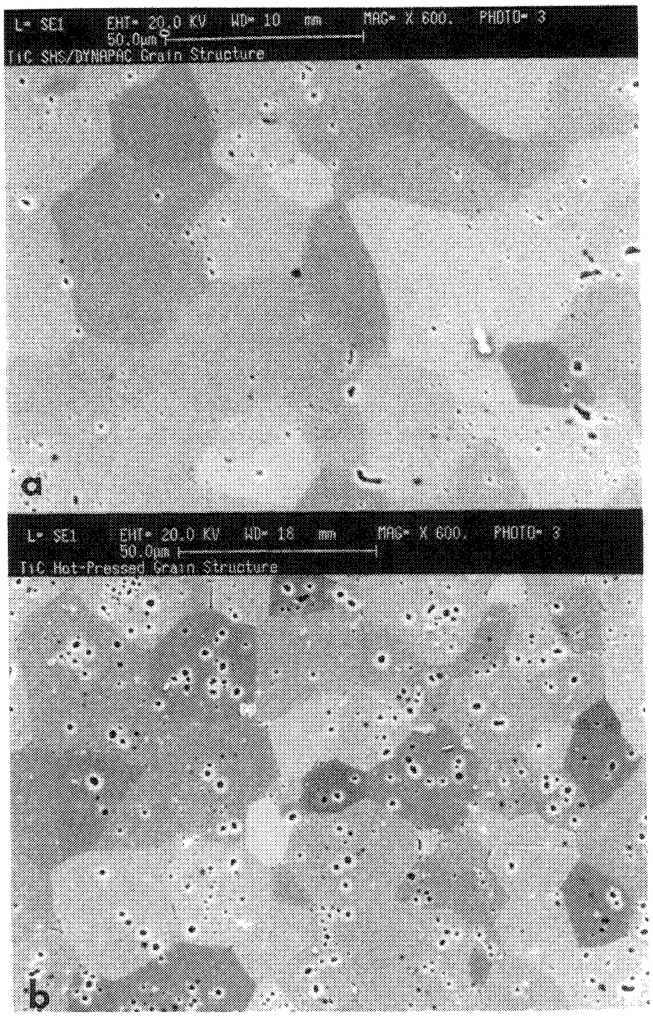

Fig. 4—Scanning electron micrographs of as-polished sections of (*a*) SHS/DC-TiC and (*b*) HP-TiC showing greater porosity in the HP-TiC material compared to SHS/DC-TiC.

exhibit an anisotropy consistent with the compressive plastic deformation process (compressive engineering strain of approximately −0.5). The grain size of the SHS/DC-TiC was determined by the linear intercept method to be ≈44 μm, while the HP-TiC grain size was ≈30 μm. The density of the SHS/DC-TiC was found to increase with increasing compaction energy, and a maximum density of 96 pct was achieved for the best conditions. The hardness of the SHS/DC-TiC was found to increase with density, as shown in Figure 3, with a maximum Vickers hardness of 2257 HVN obtained for the 96 pct dense material. The density of the HP-TiC was consistently found to be in excess of 99 pct; however, the hardness typically fell lower than the densest SHS/DC-TiC material at ≈2235 HVN.

Figure 4 shows scanning electron micrographs of polished and unetched sections of the SHS/DC- and HP-TiC's, (a) and (b), respectively. Comparison of Figures 4(a) and (b) clearly shows that the level of porosity in the SHS/DC-TiC is significantly lower than in the HP-TiC. In both TiC's, the pores were observed at grain boundaries and within grain interiors. Two pore morphologies typical of both the SHS/DC- and HP-TiC were observed: (1) large, irregularly shaped pores and (2) smaller, facetted pores. The larger pores are believed to result from the original porosity present in the green compact, while the smaller pores are likely the result of combustion gases. The smaller pores exhibited regular geometric shapes due to the anisotropy of surface energy in TiC, as shown more clearly in the fractograph of Figure 5. The observation here of a larger pore density in the HP-TiC compared to the SHS/DC-TiC is in contradiction to the density measurements discussed above. It would be expected that the higher density of the HP-TiC would be a result of a much lower porosity level; however, in fact, the opposite is true.

B. *TEM Observations and Analysis*

Figure 6 shows typical thin foil microstructures of the SHS/DC-TiC and HP-TiC, (a) and (b), respectively. The microstructures consist of equiaxed grains with numerous grain boundary voids (marked "A" in Figure 6(b)) and grain interior voids (marked "B"). Dislocations were commonly observed at the voids within the grains, as shown in Figure 7. In all cases, the dislocations observed could be shown to exist as dislocation dipoles. Figure 8 shows a micrograph of dislocations in the SHS/DC-TiC, with arrows indicating the position of apparent dislocation "pairs." The width of these dislocation pairs varied both with reversing the operative reflections (*i.e.*, ±**g**-vectors) and reversing the Bragg deviation (*i.e.*, the *s* parameter), indicating that the dislocations existed as dislocation dipoles. The dislocation dipoles were primarily edge in character, lying on {111} planes with ⟨110⟩-type Burgers vectors, as determined by the "invisibility" criteria (*i.e.*, $\mathbf{g} \cdot \mathbf{b} = 0$, in this particular case for edge dislocations, $\mathbf{g} \cdot \mathbf{b} \wedge \mathbf{u} = 0$, where $\mathbf{u}$ is the dislocation line vector[11]).

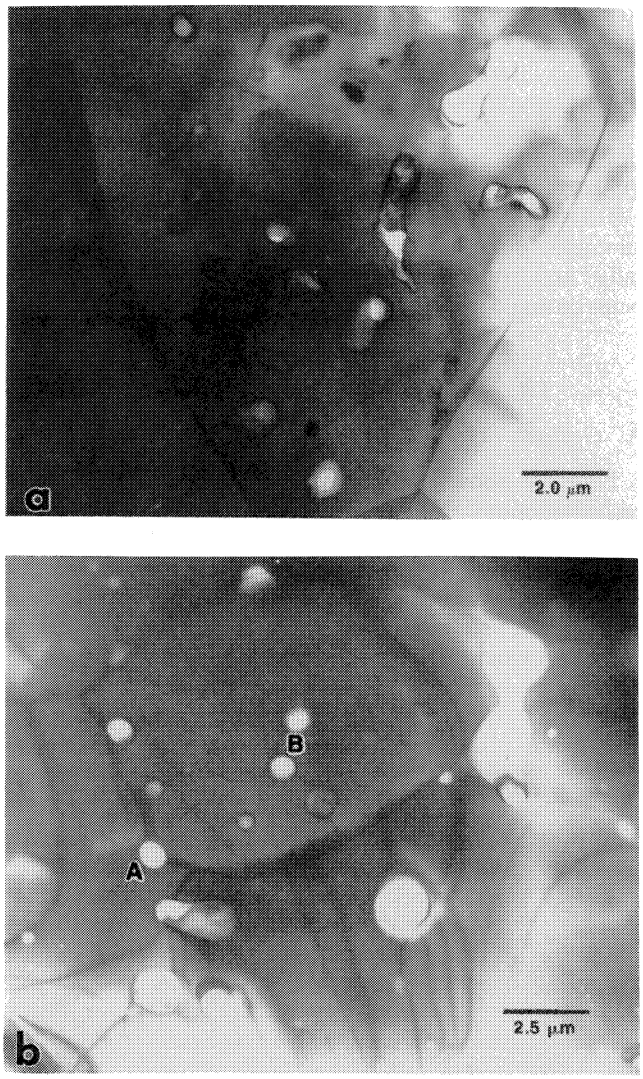

Fig. 6—Transmission electron micrograph from (*a*) SHS/DC-TiC and (*b*) HP-TiC showing the typical thin foil microstructure of each material. Voids can be observed along grain boundaries (marked "A") and within grains (marked "B") of both materials.

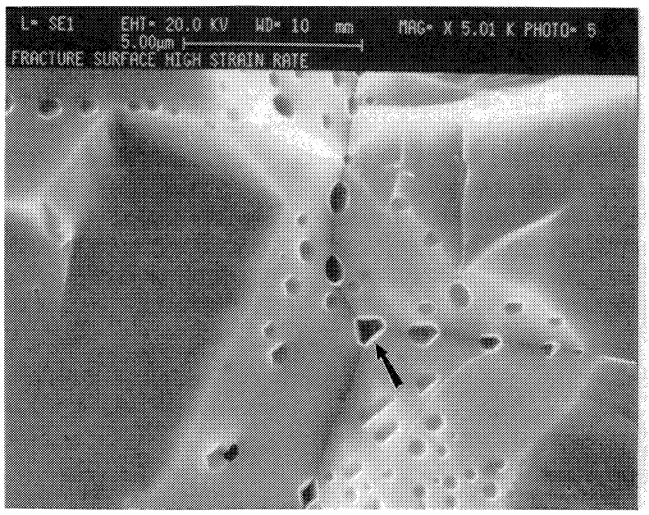

Fig. 5—Scanning electron micrograph of an intergranular, high strain rate fracture surface showing facetted voids located at grain boundaries (arrows).

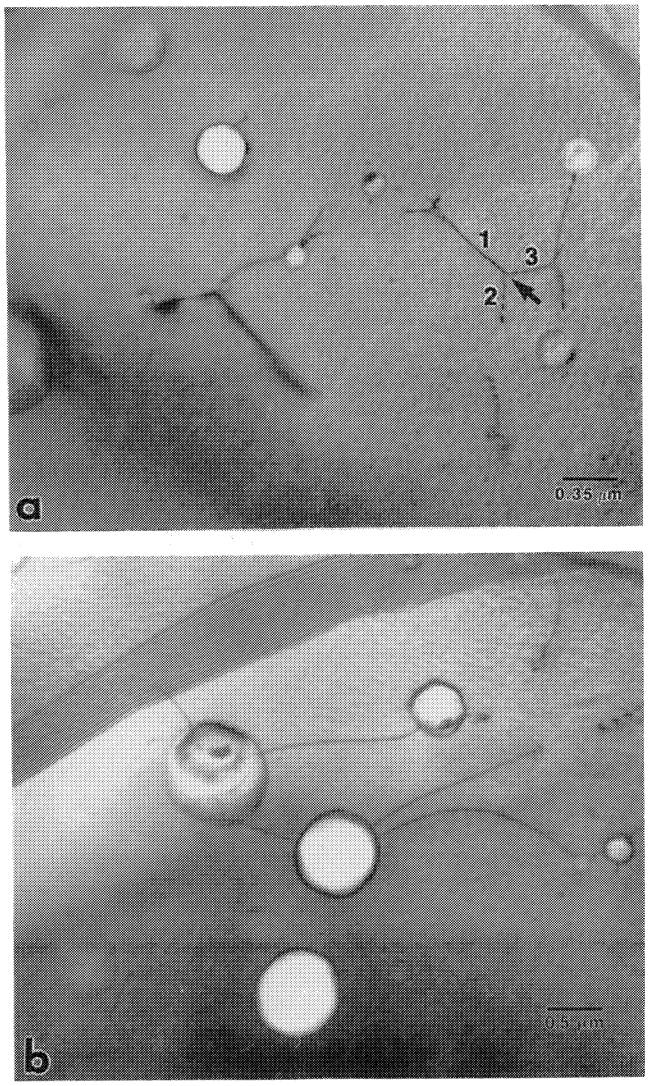

Fig. 7—Transmission electron micrograph from (*a*) SHS/DC-TiC and (*b*) HP-TiC showing dislocations pinned at voids within grain interiors. Dislocations marked "1," "2," and "3" in (a) form a dislocation network with the following Burgers vectors: $\mathbf{b}_1 = [101]$, $\mathbf{b}_2 = [01\bar{1}]$, and $\mathbf{b}_3 = [\bar{1}\bar{1}0]$.

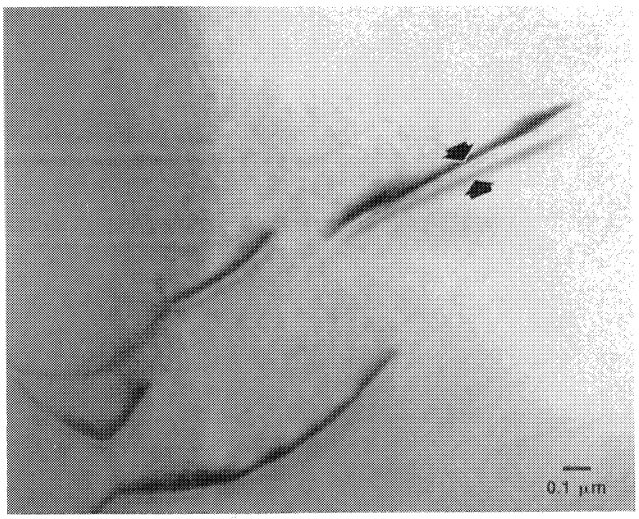

Fig. 8—Transmission electron micrograph showing dislocation dipoles typical of those observed in both TiC's.

In Figure 7(a), three dislocations are marked as 1, 2, and 3 and form a dislocation network, with each dislocation line pinned at the node indicated by the arrow. The Burgers vectors of each of these dislocations were determined to be $b_1 = [101]$, $b_2 = [01\bar{1}]$, and $b_3 = [\bar{1}\bar{1}0]$. At the node, the dislocation forces are balanced, leading to

$$b_1 + b_2 + b_3 = 0$$

The observation of $\{111\}\langle 110\rangle$-type dislocations suggests that these dislocations are introduced during the high-temperature forging operation (in the SHS/DC material) and during the hot-pressing operation (in the HP-TiC material). It has been shown by Chatterjee *et al.*[12] that in single crystals of TiC, $\{111\}\langle 110\rangle$ slip systems are only operative above 800 °C (*i.e.*, above the ductile-to-brittle transition temperature), while below 800 °C, the operative slip systems are $\{110\}\langle 110\rangle$. Much higher dislocation densities likely existed as a result of the dynamic

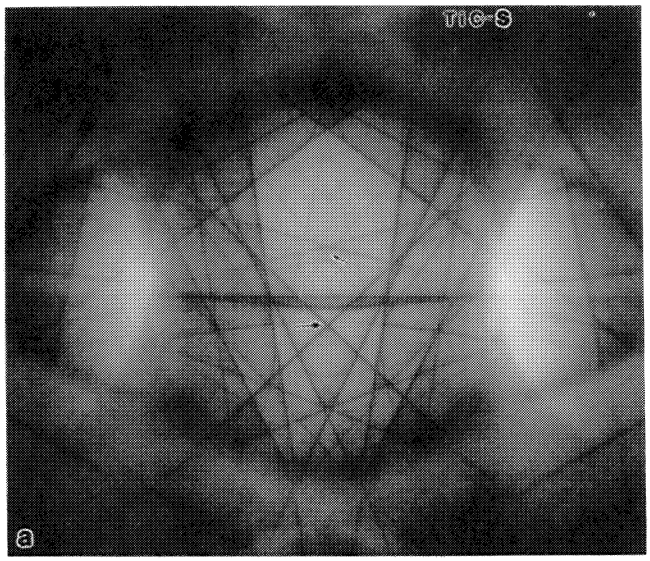

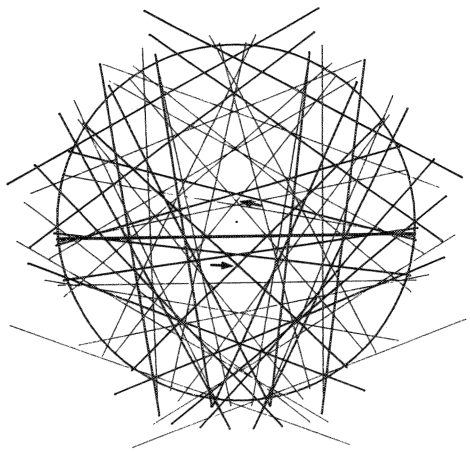

Fig. 9—(*a*) Experimental CBED HOLZ line pattern obtained from SHS/DC-TiC. (*b*) Computer simulated HOLZ line pattern which best matched the pattern in (a) for a lattice parameter of 0.4310 nm. The arrows in (a) and (b) indicate equivalent position between both patterns.

forging operation; however, the very high reaction temperature and reasonably slow cooling rate of the furnace-cooled product lead to annihilation of most of the dislocations. The few dislocations observed remain within the grains due to pinning by the pores and other dislocations, as shown in Figure 7.

The lattice parameters of both the SHS/DC-TiC and the HP-TiC were determined from CBED patterns containing HOLZ lines within the transmitted disk. The [114] crystal orientation was used throughout, and numerous individual grains in each material were analyzed to obtain typical results. The microscope accelerating voltage was determined and adjusted to be exactly 100 kV ± 200 V using a pure copper standard. This voltage was then maintained for patterns recorded from both TiC's. Figure 9 shows the experimental pattern obtained from the SHS/DC-TiC, along with a computer simulation of the HOLZ lines, which corresponds to the best match obtained. Figure 10 shows a very similar pattern obtained from the HP-TiC, along with its best match computer simulation. The lattice parameter of the SHS/DC-TiC was determined to be 0.4310 nm, and for the HP-TiC, the lattice parameter was found to be 0.4312 nm. Figure 11 shows a series of computer simulated CBED HOLZ line patterns illustrating the changes in HOLZ line positions as a function of TiC lattice parameters with a constant accelerating voltage of 100 kV. The regions contained within the small circles show the most obvious shifts in HOLZ line positions. The best matches obtained for Figures 9 and 10 were achieved by simulating patterns with changes in lattice parameters of 0.0002 nm, the experimental accuracy of the technique. As such, the lattice parameters for both TiC's can be assumed to be essentially the same within the accuracy of this technique.

The lattice parameter (a_0 = 0.4310 nm) indicates a carbon-deficient structure for TiC corresponding to a composition of approximately $TiC_{0.8}$ according to the data by Ehrlich.[13] The original green compact for the SHS/DC-TiC was prepared with a composition of $TiC_{0.9}$, indicating that some carbon was lost in the combustion process probably as gaseous CO_2 or CO. Some carbon loss apparently occurs in the preparation of the HP-TiC material; however, no details of the preparation of this material were made available.

In one sample of the SHS/DC-TiC, a small amount of thin plate-like precipitate was observed (Figure 12). The phase was determined by X-ray microanalysis to contain aluminum, oxygen, titanium, and possibly, carbon, although the latter was difficult to verify due to the extremely thin nature of the precipitate within the TiC matrix (Figure 13). The precipitate has three variants lying on {111} planes within the matrix (see the centered dark-field image of Figure 12(b)), as indicated by the streaked spots parallel to {111} matrix reflections in the diffraction pattern (Figure 13(a)). The precipitates appear highly faulted, leading to the fringes observed within the precipitate images. The morphology and diffraction

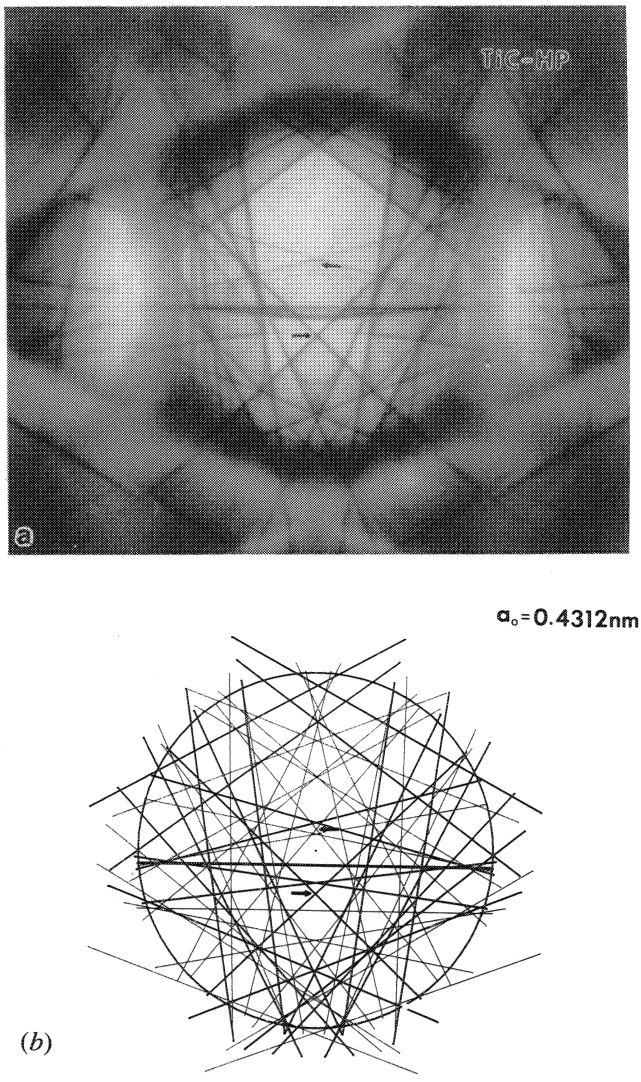

Fig. 10—(*a*) Experimental CBED HOLZ line pattern obtained from HP-TiC. (*b*) Computer simulated HOLZ line pattern which best matched the pattern in (a) for a lattice parameter of 0.4312 nm. The arrows in (a) and (b) indicate equivalent position between both patterns.

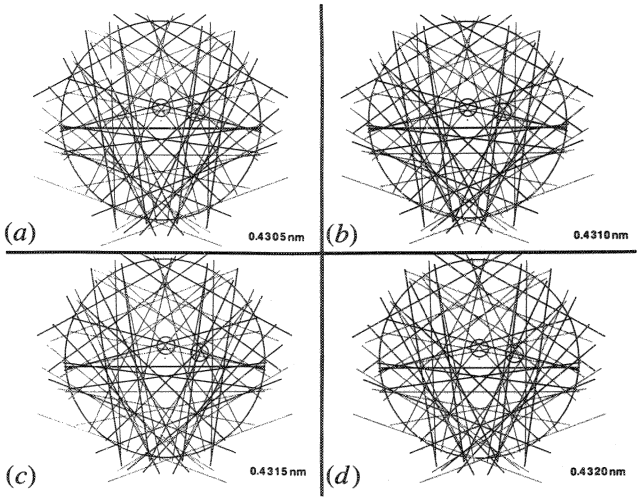

Fig. 11—(*a*) through (*d*) Series of computer simulated HOLZ line patterns for various lattice parameters for the TiC structure. The regions in each pattern defined by the small circles indicate the most obvious HOLZ line position shifts.

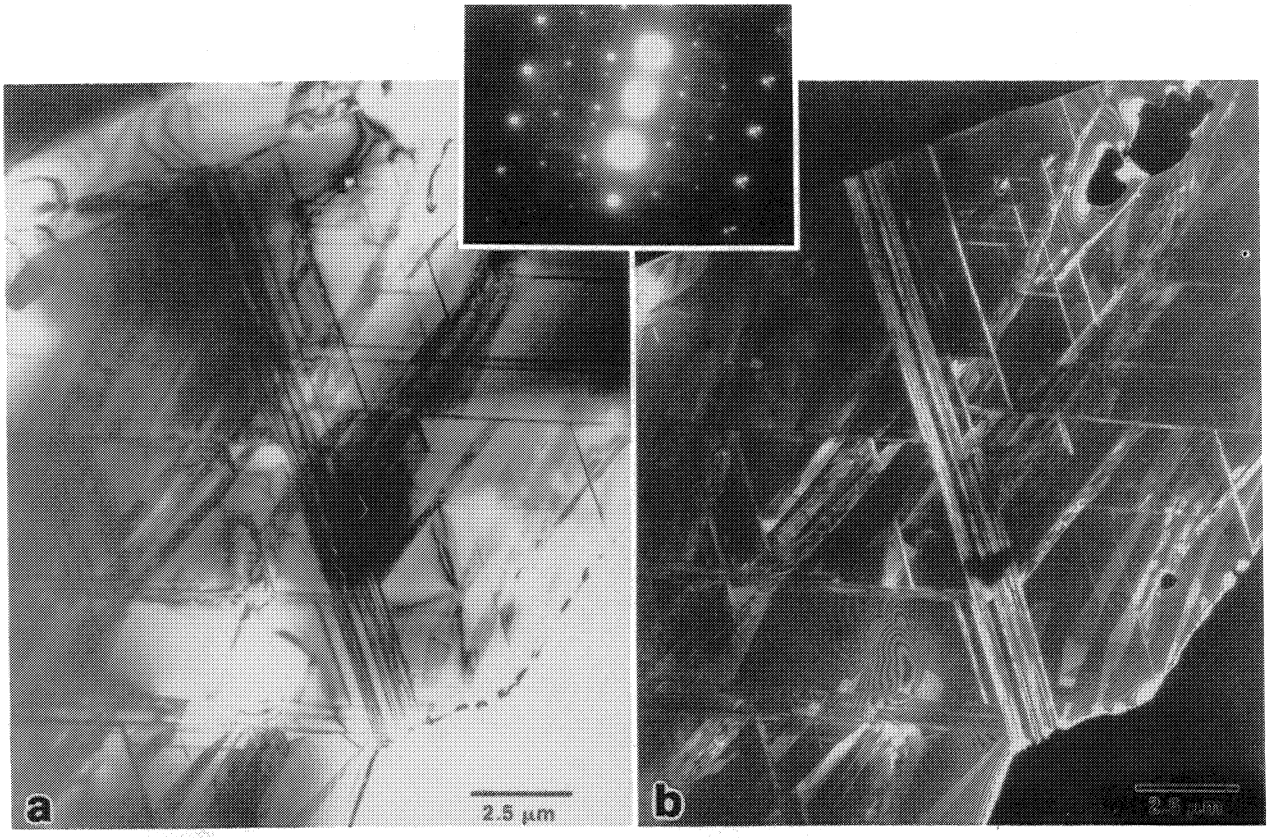

Fig. 12—(*a*) Bright-field and (*b*) centered dark-field electron micrographs of Ti-Al-O(C) precipitates in one SHS/DC-TiC. The inset shows the diffracting conditions used for these images. Three variants of this precipitate were observed lying on {111} planes.

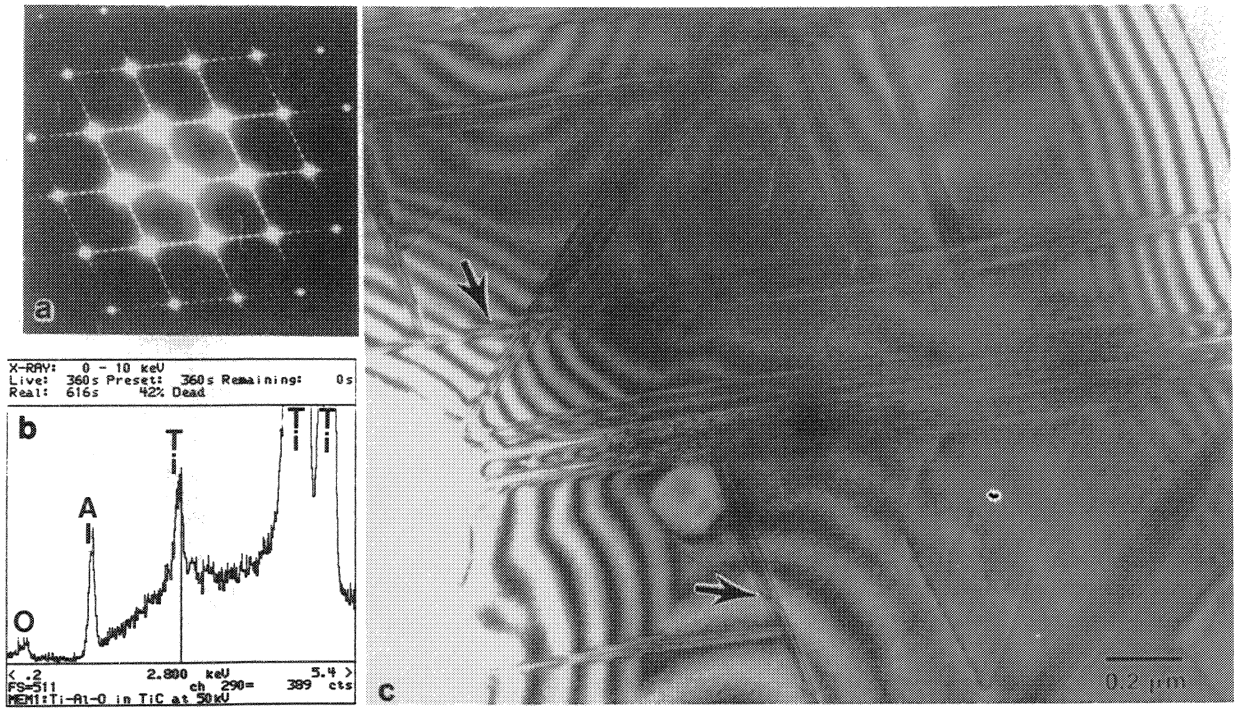

Fig. 13—(*a*) [01$\bar{1}$] zone axis diffraction pattern from SHS/DC-TiC containing thin Ti-Al-O(C) precipitates. (*b*) X-ray spectrum from precipitates shown in (c). (*c*) Bright-field electron micrograph of precipitates (arrows) for diffracting conditions given in (a). The spotted streaks in the diffraction pattern of (a) are the result of the thin nature of the precipitates and their apparently faulted structure.

information obtained from these precipitates suggest that their structure may be hexagonal ($c \approx 2.0$ nm and $a \approx 0.30$ nm), with an orientation relationship of $(0001)_{ppt} \parallel (111)_{TiC}$ and $[10\bar{1}0]_{ppt} \parallel [\bar{1}10]_{TiC}$. A few larger particles of apparently the same composition were observed along one grain boundary; however, the small size of the particles made more accurate structure determination difficult. Although no phases were found in the literature which match this structure and composition, a similar phase does exist ($AlCTi_2$) which is hexagonal ($c/a = 4.5$, space group $P6_3/mmc$).[14] A number of other similar phases exist based on the $AlOCr_2$ prototype structure (space group $P6_3/mmc$), such as $AlCV_2$, AlCTaTi, and AlCTiV.[14] Based on this information, the

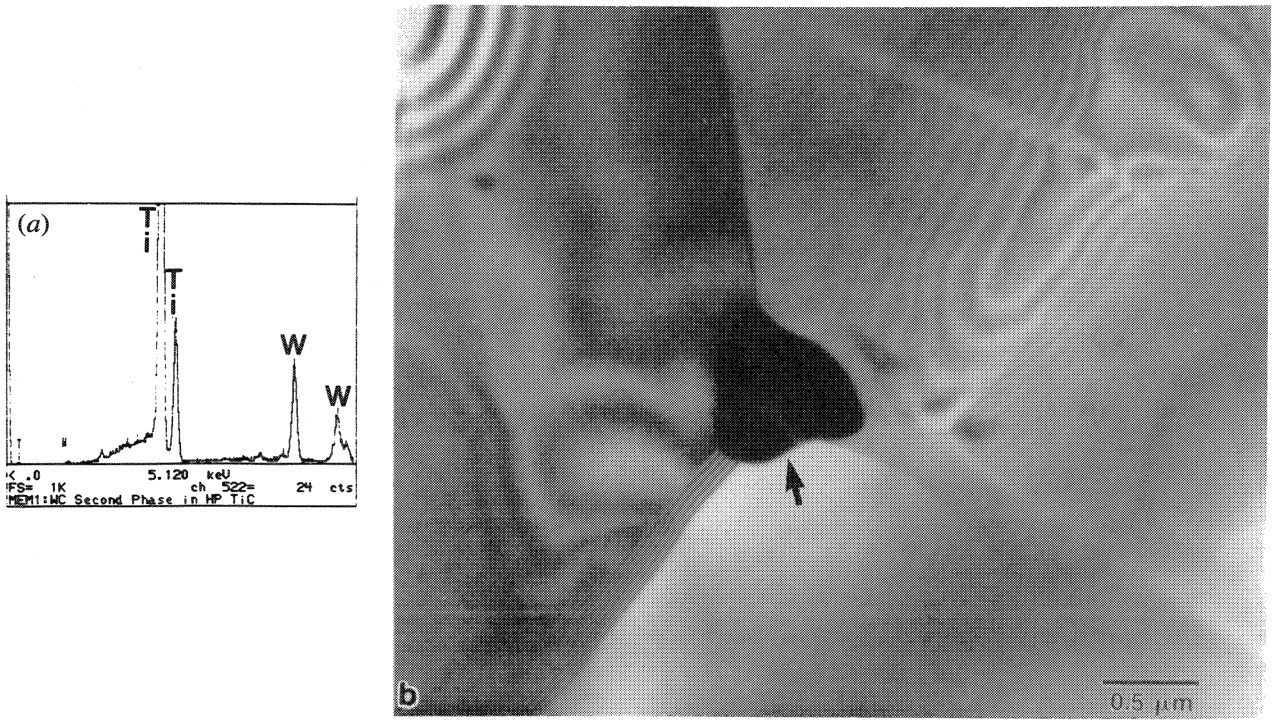

Fig. 14—(*a*) X-ray spectrum and (*b*) Bright-field electron micrograph of Ti(W)-carbides located at a triple point in the HP-TiC material.

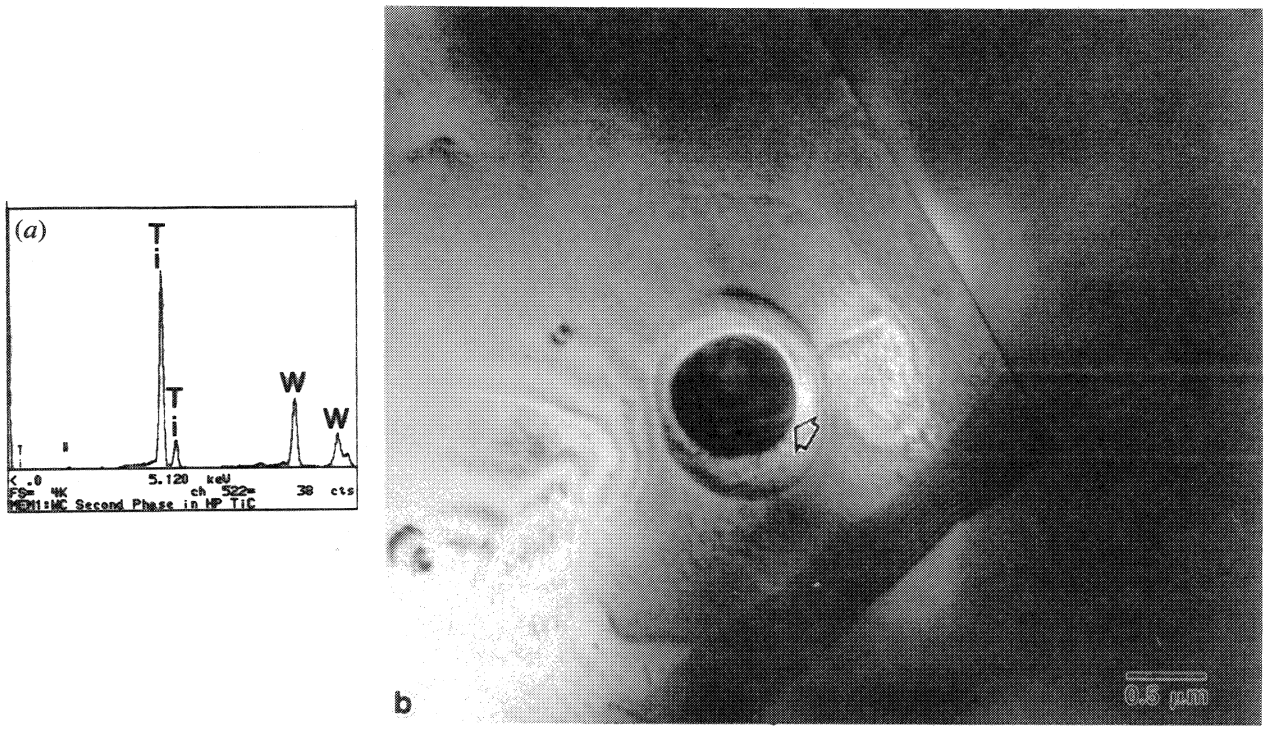

Fig. 15—(*a*) X-ray spectrum and (*b*) Bright-field electron micrograph of Ti(W)-carbides located within grain interiors of the HP-TiC material.

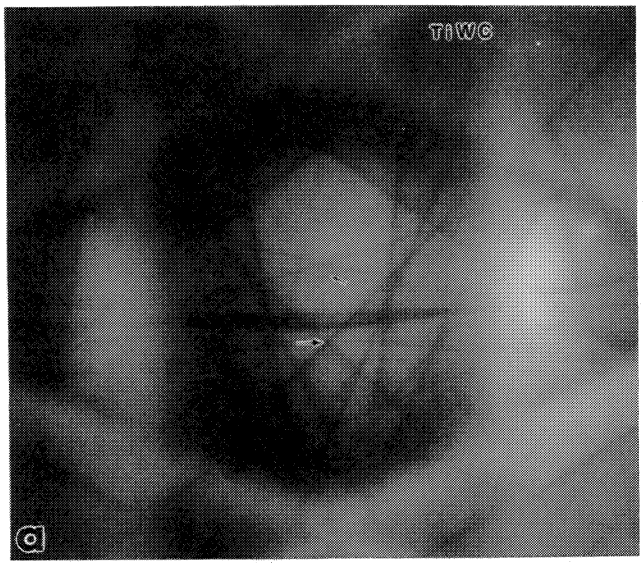

(*b*)

Fig. 16—(*a*) Experimental CBED HOLZ line pattern obtained from Ti(W)-carbides observed in the HP-TiC. (*b*) Computer simulated HOLZ line pattern which best matched the pattern in (a) for a lattice parameter of 0.4305 nm. The arrows in (a) and (b) indicate equivalent position between both patterns.

composition of this phase is likely Al-C_x-$O_{1-x}Ti_2$, having the $AlOCr_2$ prototype structure.

This phase [$AlO(C)Ti_2$] is believed to have been formed as the result of the introduction of a small amount of alumina (Al_2O_3) into the original green compact. The starting titanium and carbon powders are mixed in a ball mill with Al_2O_3 spheres in order to reduce the amount of agglomeration as well as to provide a homogeneous mixture of the two powders. It is likely that a small fragment from the Al_2O_3 spheres broke off and remained in the powder mixture. Subsequently, this new phase was formed during the SHS process or precipitated out during furnace cooling of the reacted product.

The HP-TiC microstructure contained a large concentration of two types of second-phase particles located both at grain boundaries and within grains. The most common particles were tungsten-based and observed at grain boundaries, triple points (Figure 14), and within grains, as shown in Figure 15. The particles contained significant amounts of both tungsten and titanium, in approximately equal amounts, with no other elements detected. The structure of these particles was determined by CBED to be cubic (NaCl-prototype), having a lattice parameter of 0.4305 nm. Figure 16 shows the CBED HOLZ line pattern obtained from these Ti-W particles, along with a computer simulation of the best matched HOLZ line pattern. These particles are likely Ti(W)-carbides which form from W impurities in the starting powders. The lack of any carbon X-ray peaks in the spectra from these particles is due to the increased absorption created by the high tungsten composition. Tungsten carbide (WC) can also possess the NaCl-structure at very high temperatures (a_0 = 0.4336 nm). The addition of titanium to WC likely stabilizes the NaCl structure at lower temperatures and produces a more carbon-deficient ternary carbide [Ti(W)C] which would account for the lower lattice parameter of this phase compared to the TiC. No phases of this type could be found in the literature; however, Table I shows a list of some of the known carbides that form with the NaCl-structure possessing lattice parameters between 0.3 and 0.6 nm. From this vast array of similar carbides, it can readily be expected that this ternary carbide should exist.

The second type of particles that was found in the HP-TiC was observed only along grain boundaries and triple points. Figure 17 shows a micrograph and accompanying X-ray spectrum of one such particle. The X-ray spectrum reveals that these particles contain Ti, Co, and Fe. Similar particles were observed by Katz *et al.*[15] in hot-pressed TiC produced from powders obtained from Starke, Inc. They concluded that these particles were likely carbides; however, no structure determination was conducted. In the present study, the structure of these particles was determined by CBED, and they were shown to possess the NaCl-structure as well. Figure 18 shows the CBED HOLZ line pattern obtained from these particles, along with the computer simulated pattern for a lattice parameter of 0.430 nm. These particles are likely Ti(Co) (Fe)-carbides, again producing a somewhat carbon-deficient structure, as indicated by the low lattice parameter.

In addition to the second-phase particles discussed above, many of the voids observed in the HP-TiC material, both within grains and along boundaries, were analyzed. In many cases, small amounts of either tungsten or iron and cobalt were detected along the periphery of the holes, suggesting that some of these voids previously contained particles which were extracted during polishing. This indicates that the actual porosity level of the HP-TiC material may be lower than observed in the SEM (Figure 4(b)).

The observation of large quantities of second-phase particles in the HP-TiC material and the fact that these particles possess rather heavy elements, such as W or Fe-Co, suggest that the higher density of this material results, at least in part, from these particles. Since no such particles were observed in the SHS/DC-TiC, the measured density of this material better reflects the true density of TiC and the remnant porosity as produced by

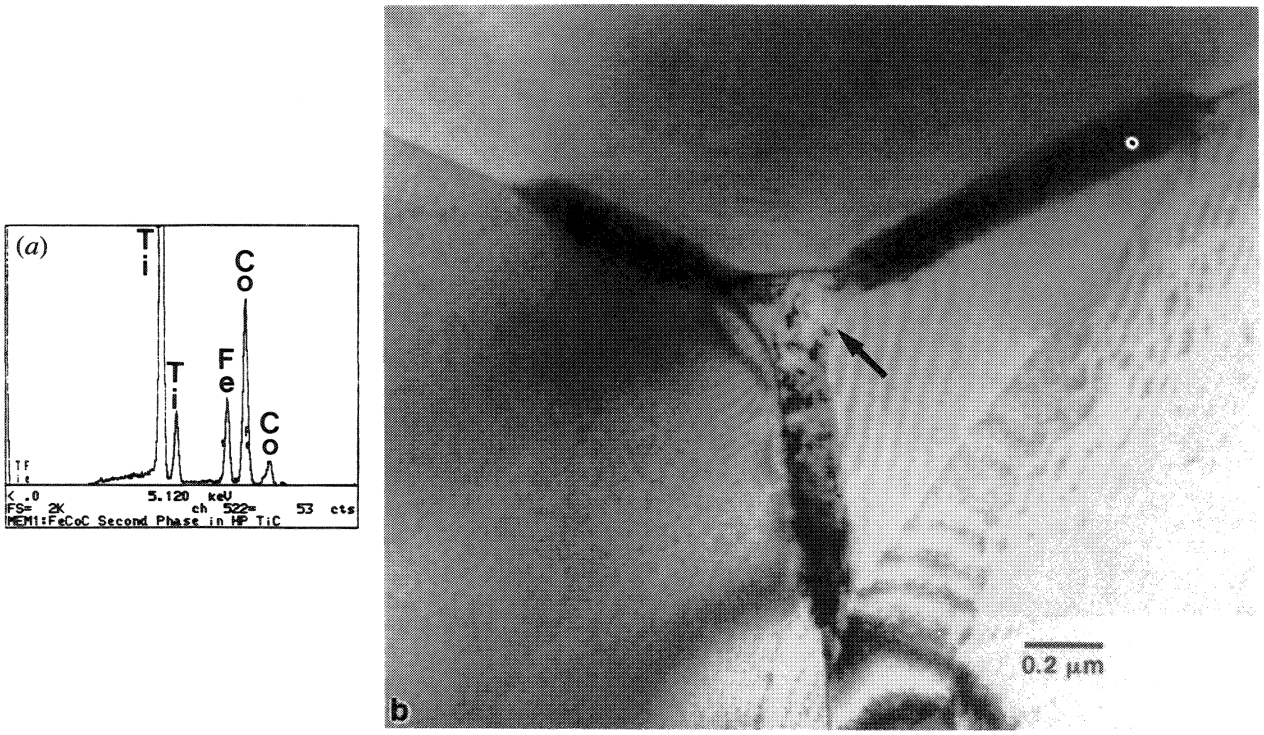

Fig. 17—(*a*) X-ray spectrum and (*b*) Bright-field electron micrograph of Ti(Fe)(Co)-carbides located at a triple point in the HP-TiC material.

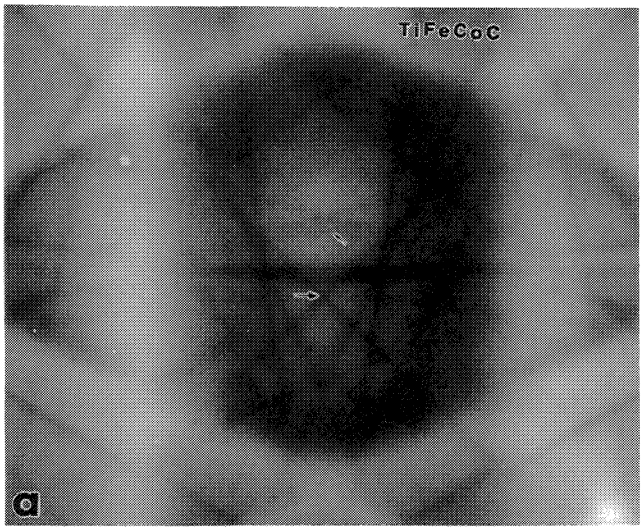

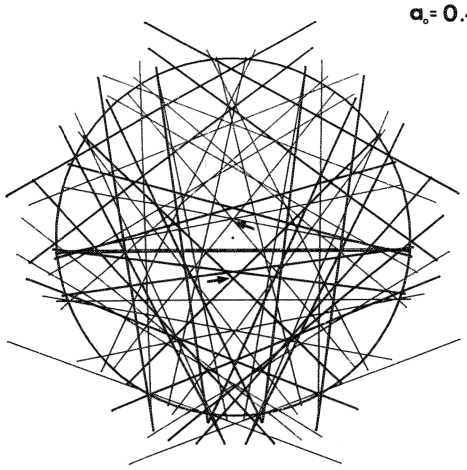

Fig. 18—(*a*) Experimental CBED HOLZ line pattern obtained from Ti(Fe)(Co)-carbide in Fig. 17(b). (*b*) Computer simulated HOLZ line pattern which best matched the pattern in (a) for a lattice parameter of 0.4305 nm. The arrows in (a) and (b) indicate equivalent position between both patterns.

Table I. List of Some of the Known Carbides Possessing the NaCl-Structure Having Lattice Parameters between 0.3 and 0.6 nm[14]

Carbides with NaCl Structures (Space Group Fm3m, Number 225)	
Carbide	a_0
C_2Ca	0.5886
C-Ce-N-Th	0.520
C-Ce-U	0.4972
CCr	0.362
C-Cr-Ti	0.4299
C-Cr-Ti-W	0.4258
C-Cr-V	0.4575
C-Dy-N-Th	0.512
C_2Er_3	0.50214
C-Er-N-Th	0.519
C-Fe-Ti	0.4308
CGd_3	0.5126
C-Gd-N-Th	0.516
C-H-Hf	0.4647
C-H-Li	0.4096
C-H-Nb	0.4448
C-H-Ti	0.4326
C-H-V	0.4138
C-H-Zr	0.4661
C-Hf	0.4638
C-Hf-Mo	0.437
C-Hf-N	0.4565
C-Hf-N-Nb	0.447
C-Hf-N-Ta	0.449
C-Hf-N-Ti	0.436
C-Hf-N-Zr	0.458
C-Hf-N-Zr	0.460
C-Hf-Nb	0.4545
C-Hf-Nb-U	0.467
C-Hf-Nb-V	0.447
C-Hf-Ta	0.4543
C-Hf-Ta-U	0.466
C-Mo-Ti	0.4284
C-Mo-V	0.4235

Table I. Cont. List of Some of the Known Carbides Possessing the NaCl-Structure Having Lattice Parameters between 0.3 and 0.6 nm[14]

Carbides with NaCl Structures (Space Group Fm3m, Number 225)	
Carbide	a_0
C-Mo-W	0.4237
C-V-W	0.421
CW	0.4336
C-Th-U	0.345
C-Ti	0.43176

this method. On the other hand, the measured density of the HP-TiC reflects the combination of TiC, high density, second-phase particles, and remnant porosity of the hot-pressing process.

IV. CONCLUSIONS

Titanium carbide produced by combustion synthesis followed by rapid densification in a high-speed forging machine was characterized and compared with TiC produced by hot pressing. The density of the combustion-synthesized/dynamically compacted TiC reached values greater than 96 pct of theoretical density, while commercially produced hot-pressed TiC typically exceeded 99 pct. The microstructures of both TiC's consist of equiaxed TiC grains, with some porosity located both at grain boundaries and within grain interiors. In both cases, SHS/DC and hot-pressed, the TiC is ordered cubic (NaCl-structure, B_1; Space Group Fm3m) with a lattice parameter of $\approx$0.4310 nm, indicative of a slightly carbon-deficient structure. In one SHS/densified specimen, a new, complex Ti-Al-O(C) phase was observed at a grain boundary as small, rod-like particles, as well as within certain grains as thin, plate-like precipitates. The structure of this phase is believed to be hexagonal, with a c-axis/a-axis ratio of $\approx$6.6, similar to the $AlCTi_2$ phase which has a point group 6 mmm. In all other SHS/densified TiC samples, the grains and grain boundaries were devoid of any second-phase particles. The hot-pressed TiC exhibited a greater degree of porosity than the SHS/densified specimens and a large concentration of second-phase particles at grain boundaries and within grains. The structure and composition of these second-phase particles were determined by CBED and X-ray microanalysis to be Ti(W)-carbides and Ti(Co)(Fe)-carbides. The additional mass resulting from these second-phase particles likely accounts for the higher density measured for the hot-pressed material, even in the presence of apparently higher levels of porosity.

ACKNOWLEDGMENTS

This research was supported by the Army Research Office under Contract No. ARO-DAAL-03-88-K-0194. We also thank Mr. Richard Policka, President, CERCOM, Inc., for his assistance in supplying the hot-pressed TiC. One of the authors (GTG) acknowledges support by the United States Department of Energy.

REFERENCES

1. A.G. Merzhanov, V.M. Shkiro, and I.P. Borovinskaya: U.S. Patent 3,726,643, 1973.
2. N.P. Novikov, I.P. Borovinskaya, and A.G. Merzhanov: in *Combustion Processes in Chemical Technology and Metallurgy*, A.G. Merzhanov, ed., Chernogolvka, USSR, 1975 (English translation).
3. A.G. Merzhanov: in *Combustion and Plasma Synthesis of High-Temperature Materials*, Z.A. Munir and J.B. Holt, eds., VCH Publishers, New York, NY, 1990, pp. 1-53.
4. W.L. Frankhouser, K.W. Brendley, M.C. Kieszek, and S.T. Sullivan: *Gasless Combustion Synthesis of Refractory Compounds*, Noyes Publications, Park Ridge, NJ, 1985.
5. Z.A. Munir and U. Anselmi-Tamburini: *Mater. Sci. Rep.*, 1989, vol. 3, pp. 277-365.
6. J. LaSalvia, L.W. Meyer, M.A. Meyers, and A. Niiler: in *Shock-Wave and High-Strain-Rate Phenomena in Materials*, M.A. Meyers, L.E. Murr, and K.P. Staudhammer, eds., Marcel Dekker, 1992, in press.
7. L.W. Meyer, J.C. LaSalvia, and M.A. Meyers: University of California, San Diego, La Jolla, CA, unpublished research, 1991.
8. A. Niiler, L.J. Kecskes, and T. Kottke: in *Combustion and Plasma Synthesis of High-Temperature Materials*, Z.A. Munir and J.B. Holt, eds., VCH Publishers, New York, NY, 1990, pp. 309-14.
9. D.A. Hoke, M.A. Meyers, L.W. Meyer, and G.T. Gray III: *Metall. Trans. A*, 1992, vol. 23A, pp. 77-86.
10. K.S. Vecchio: in *Microbeam Analysis—1989*, P.E. Russell, ed., San Francisco Press, San Francisco, pp. 477-79.
11. J.W. Edington: in *Practical Electron Microscopy in Materials Science*, Interpretation of Transmission Electron Micrographs, N.V. Philips' Gloeilampenfabrieken, Eindhovaen, 1975, vol. 3.
12. D.K. Chatterjee, M.G. Mendiratta, and H.A. Lipsitt: *J. Mater. Sci.*, 1979, vol. 14, p. 2151.
13. P. Ehrlich: *Z. Anorg. Chem.*, 1949, vol. 1, p. 259.
14. P. Villars and L.D. Calvert: *Pearson's Handbook of Crystallographic Data for Intermetallic Phases*, ASM, Metals Park, OH, 1985, vol. 2.
15. A.P. Katz, H.A. Lipsitt, T. Mah, and M.G. Mendiratta: *J. Mater. Sci.*, 1983, vol. 18, pp. 1983-92.